A multigrid Waveform Relaxation Method for solving the Pennes bioheat equation

Cosmo D. Santiago, Gylles R. Ströher, Marcio A. V. Pinto & Sebastião R. Franco

Published online: 06 Jan 2023.

Submit your article to this journal ⟶

Article views: 38

View related articles ⟶

View Crossmark data ⟶

Taylor & Francis
Taylor & Francis Group

Check for updates

A multigrid Waveform Relaxation Method for solving the Pennes bioheat equation

Cosmo D. Santiago[a] , Gylles R. Ströher[b] , Marcio A. V. Pinto[c] , and Sebastião R. Franco[d]

[a]Department of Mathematics, Federal Technological University of Paraná, Apucarana, Paraná, Brazil;
[b]Chemical Engineering Coordination, Federal Technological University of Paraná, Apucarana, Paraná, Brazil;
[c]Department of Mechanical Engineering, Federal University of Paraná, Curitiba, Paraná, Brazil; [d]Department of Mathematics, State University of Centro-Oeste, Irati, Paraná, Brazil

ABSTRACT

This work proposes a multigrid Waveform Relaxation Method (WRMG) that uses the finite difference method for the discretization to solve Pennes' bioheat equation. There is no evidence in the literature of using the WRMG to solve this equation. The proposed algorithm is based on the red-black Gauss-Seidel smoother in space and the line Gauss-Seidel smoother in time. Verification of code is presented. The performance analysis of the multigrid method confirms the convergence and efficiency of the algorithm. The method, which favors parallel architecture, is tested in two-dimensional numerical experiments on an academic problem and for the thermal analysis of human skin.

1. Introduction

Changes in skin temperature have been used to diagnose human anomalies since the dawn of civilization. The study of heat transfer in human tissues is becoming an increasingly helpful tool for treatments and the diagnosis of cancers. According to Anbar [1], prehistoric healers have observed that the affected skin region of an injury or wound shows an increase in temperature. Over the past 50 years, significant progress has been made in noninvasive thermal diagnoses of melanomas with the development of more accurate body thermal mapping devices, mathematical models, and numerical techniques for solving partial differential equations and thus, thermal image processing.

As stated in [2, 3], highly vascular cancerous lesions on the skin, such as melanomas, can increase blood perfusion and the local rate of metabolic heat generation, which leads to a higher temperature in that skin region than in the healthier surrounding areas. This difference in temperature can assist in diagnosing melanomas and other skin lesions. However, according to [4–6], the temperature increase due to melanoma is relatively small in steady-state cases, that is, cases with a nondynamic heat transfer condition. Therefore, equipment with high thermal sensitivity is required for more accurate measurement, especially for early detection and deeper lesions.

Alternatively, Dynamic Thermal Imaging (DTI) can be used to thermally map the skin region in question, which consists in applying a thermal stimulus before generating the image to increase

Nomenclature

c	specific heat at isobaric conditions		ν_1	inner interactions in restriction
h	distances between two consecutive points in the grid		ν_2	inner interactions in prolongation
			ρ_m	average convergence factor
k	thermal conductivity		ρ	density
L	number of levels		ω	blood perfusion rate
N	total number of spatial points in the grid or time		**Subscripts**	
			a	arterial blood
q	heat source		b	blood
R	residue in linear system		ext	external heat source
T	tissue temperature		met	metabolic heat generation
t	time		t	tissue
X	x direction			
Y	y direction		**Superscript**	
			0	initial estimate
			it	it-th iteration

Greek symbols

ℓ	domain length
λ	degree of anisotropy

the temperature differences between the lesion area and the surrounding skin. Several researchers have studied the application of dynamic infrared in skin neoplasms as a complementary tool to increase the accuracy of the diagnostic, resulting in less stress and discomfort to the patient [7].

Herman [8] tested 37 patients with suspected skin cancer lesions using infrared dynamics and dynamic image processing. Three of the 37 lesions were cancerous (determined by biopsy) and were successfully detected using Quantification Analysis of Induced Thermography (QUAINT). According to the author, the measurement and computational hardware and the computational imaging and modeling tools have reached the maturity needed to enable accurate Quantitative infrared imaging (QUIRI), which opens new avenues in medical diagnosis, monitoring, and care.

In Godoy et al. [9], the thermal recovery curves of the suspected lesions are utilized in the context of the continuous-time detection theory to define an optimal statistical decision rule so that the algorithm's sensitivity is guaranteed to be at a maximum for every prescribed false-alarm probability. The proposed methodology was tested in a pilot study with 140 human subjects demonstrating more than 99% sensitivity for a prescribed specificity above 99% for skin cancer detection. The authors argue that a standardized analysis method for DTI has the potential to reduce the number of biopsies performed on suspicious lesions significantly.

Moreover, many authors [7, 10] have studied using the abnormal temperature of the skin surface to predict the location, size, and thermal parameters of the tumor or types of skin neoplasia. In general, this approach considers two different inverse problems. The first problem is about the location: depth, width, and size of the tumor, assuming all other parameters are known. The second one discusses estimating the metabolic heat source intensity inside the tumor region once the tumor's radius and its center's location are known [10, 11].

In both cases, given the temperature profiles obtained in the simulations, different methodologies can be used to analyze the clinical data. In addition, an optimization algorithm such as the Genetic Algorithm [12], Ant Colony [13], BGOA [14], or Pattern Search method [15] can be used to estimate the tumor's parameters by minimizing a fitness function. The fitness function correlates the given data to the temperature profile for a set of estimated parameters.

In recent years, deep learning models (DLM) have been used to estimate the thermophysical properties of skin tumor, including tumor depth and size (length, width, and height), heat generation, thermal conductivity, and blood perfusion, using the temperature measured on the skin surface. A critical step in this approach is to generate the model's training samples. In many

studies, the time-dependent skin surface temperature was achieved using numerical simulation. [10] used 18,900 samples with different thermophysical properties to train the deep learning model to estimate the thermophysical properties of skin tumors.

One of the disadvantages of these inverse problems is the computational processing time since the optimization algorithms evaluate the fitness function hundreds or thousands of times, or thousands of samples are necessary to train an Artificial Neural Network (ANN), which implies the degree of grid refinement necessary for a fast numerical resolution of the bioheat problem. As tumor regions can be relatively small and an early medical diagnostic by thermal imaging is desired to be as accurate and fast as possible, a highly refined grid and a short computational processing time are desired. Rossi et al. [16] state that the duration of the simulation is a critical factor in making bioheat simulation tools clinically relevant, which motivates us to explore multi-grid methods [17, 18] in biothermal systems.

Additionally, advancements made toward understanding bioheat transfer have benefited the design and optimization of therapeutical procedures such as laser surgery, cryotherapy, magnetic nanoparticle-based hyperthermia, and radiofrequency ablation [19]. However, none of these studies employ the multigrid method.

The use of the multigrid method for the Pennes model has become more prevalent in recent years since it satisfies the requirement of a highly refined grid [5, 20–22].

Solving large linear systems resulting from discretization is the most time-consuming part of real simulations [17], and this is especially true for the Pennes bioheat equation [5]. Hence, the design of efficient solvers for this type of problem has raised much interest. Moreover, current computer architectures allow better multiprocessing capabilities by having more cores and hardware threads per chip. In order to exploit these characteristics, it is necessary to develop algorithms capable of efficiently using a large number of cores, increasing the need for parallel computing [23]. Typical solution algorithms for time-dependent problems are based on a time-marching approach [5, 20–22], in which each time step is sequentially solved. However, these traditional methods, known as Time-Stepping methods, do not allow the parallelization of the temporal variable [23], which leads researchers to seek an increase in concurrency by using time-parallel methods. From the current time parallel techniques [23], we considered a multigrid Waveform Relaxation algorithm (WRMG) [24, 25] based on a red-black Gauss-Seidel smoother in space and line Gauss-Seidel smoother in time [23]. The WRMG is being applied to solve heat transfer problems in recent years [25–29].

In this study, we propose the use of the Waveform Relaxation, a parallelizable method [25], associated with the geometric multigrid method for the 2-D Pennes' bioheat transfer equation. This article's novelty is the use of this association for to get highly accurate solutions in the shortest possible computational time.

As a result, this work may offer guidelines for medical procedures that use heat to treat and detect tumors using the spatial distribution of temperature in the thermal analysis of human skin. The high accuracy of the numerical solution of the skin temperature can also assist in verifying the temperature increase in regions with small melanomas, allowing for early diagnoses. Importantly, we would like to highlight that we have not found in literature studies on the WRMG designed for the Pennes' bioheat equation.

2. Mathematical and numerical models

2.1. Pennes bioheat equation

The first thermal mathematical model to describe heat transfer in human tissue, including the effects of blood flow on tissue temperature, was proposed by Pennes [30] in 1948. This model is

known as Bioheat Transfer Equation (BTE), Pennes Equation, or Parabolic Model. The latter is because of the mathematical classification of the differential equation used in the model.

As mentioned in [31], the BTE model was initially developed to predict heat transfer in the human forearm. Due to its simplicity, its use has extended to various biological studies. In [31–33], numerical thermal simulations for the human head were investigated. Several authors [34–38] have applied the BTE model to study and evaluate temperature changes in human breasts due to the presence of tumors. Other researchers [6, 39–42] have also applied the BTE model to study heat transfer in human skin. Numerous other works can be found in the literature to exemplify the applications of the BTE model.

The BTE model establishes the blood effect as an isotropic source or a heat sink proportional to the blood flow rate and the difference between the body's core temperature and the local tissue temperature. In other words, the model describes the effects of metabolism and blood perfusion on the tissue energy balance. These two effects were incorporated into the classic heat diffusion equation, resulting in:

$$\rho_t c_t \frac{\partial T}{\partial t} = \nabla.(k\nabla T) + \omega_b \rho_b c_b (T_a - T) + q_{met} + q_{ext}, \tag{1}$$

where T is the tissue temperature; T_a, the arterial blood temperature; k, the thermal conductivity; q_{met}, the metabolic heat generation; q_{ext}, the external heat source for spatial heating; ρ_t, the tissue density; c_t, the tissue's specific heat at isobaric conditions; ω_b, the blood perfusion rate; ρ_b, the blood density; and c_b, the blood's specific heat at isobaric conditions.

This mathematical model is given by a two-dimensional domain corresponding to the region in which it is desired to simulate the temperature distribution in human skin, defined by $\left\{ (x,y) \in R^2, 0 \le x, y \le \ell \right\}$, as seen in Figure 1.

For the numerical verification step, we used the analytical solution given by Lin and Li [40], which initial condition is $T(x, y, t = 0) = 37 \ ^oC$, Dirichlet condition on the boundary Γ_1, $T(x, y = 0, t) = 100[1 - u(t - 15)]$, here u is the step function and, adiabatic thermal conditions, $\partial T/\partial n = 0$, on the boundaries $\Gamma_{2,3,4}$. Whilst for the case study, we used adiabatic thermal conditions on the boundaries $\Gamma_{1,2,3,4}$.
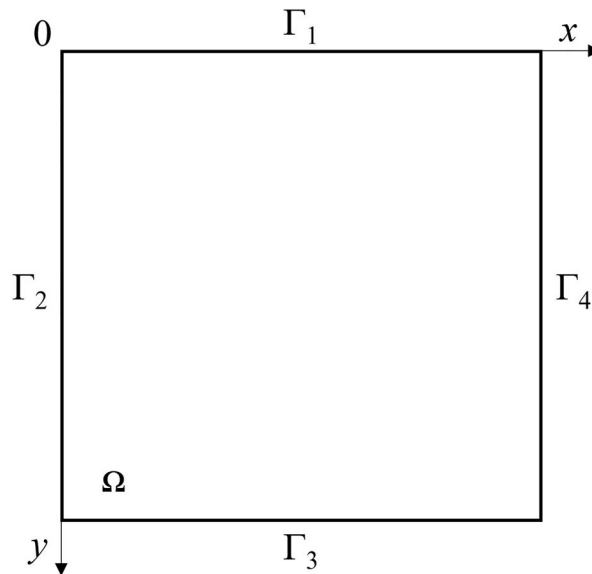
Figure 1. Computational domain and boundaries condition.

2.2. Discretization of the mathematical model

The mathematical model is discretized on the 2-D computational domain, shown in Figure 1. This domain is partitioned into several nodes (or points), given by $N = N_x N_y$, where N is the total number of spatial points in the grid, N_x and N_y are the number of points in each spatial direction, and ℓ is the domain length in both directions. A generic point P is located on the grid as $(x_i, y_j) = ((i-1)h_x, (j-1)h_y)$, in which $h_x = \ell/(N_x - 1)$, $h_y = \ell/(N_y - 1)$, $i = 1, \cdots, N_x$, $j = 1, \cdots, N_y$, and h_x and h_y are the distances between two consecutive points in the grid in the x and y directions, respectively. This work considers $h_x = h_y = h$, that is, an isotropic grid.

In order to obtain the linear system, the derivatives of Eq. (1) were approximated using the Finite Difference Method (FDM) in a uniform grid, with a five-point second-order central difference scheme accurate in space and the implicit Crank-Nicolson scheme in the temporal derivative. After the numerical approximations, Eq. (1) can be written as

$$\frac{T_P^{n+1} - T_P^n}{\Delta t} = \frac{1}{2}\left(\frac{\eta_1}{h^2}T_E^{n+1} + \frac{\eta_1}{h^2}T_W^{n+1} + \frac{\eta_1}{h^2}T_N^{n+1} + \frac{\eta_1}{h^2}T_S^{n+1} - \frac{4\eta_1}{h^2}T_P^{n+1} - \eta_2 T_E^{n+1}\right)$$
$$+ \frac{1}{2}\left(\frac{\eta_1}{h^2}T_E^n + \frac{\eta_1}{h^2}T_W^n + \frac{\eta_1}{h^2}T_N^n + \frac{\eta_1}{h^2}T_S^n - \frac{4\eta_1}{h^2}T_P^n - \eta_2 T_E^n\right) + \eta_2 T_a + \eta_3, \quad (2)$$

where $\eta_1 = k/(\rho_t c_t)$, $\eta_2 = w_b c_b \rho_b/(\rho_t c_t)$, and $\eta_3 = (q_{met} + q_{ext})/(\rho_t c_t)$, $\Delta t = t_f/(N_t - 1)$ represents the time step size, t_f is the final time, and N_t is the number of steps in time. The indices $E = (i+1, j)$, $W = (i-1, j)$, $N = (i, j+1)$, and $S = (i, j-1)$ are the nearest neighbors to the point $P = (i, j)$ in the directions x and y of the grid. With some more adjustments, Eq. (2) becomes

$$\left(\frac{1}{\Delta t} + \frac{2\eta_1}{h^2} + \frac{\eta_2}{2}\right)T_P^{n+1} = \frac{\eta_1}{2h^2}\left(T_E^{n+1} + T_W^{n+1} + T_N^{n+1} + T_S^{n+1}\right) + \frac{\eta_1}{2h^2}\left(T_E^n + T_W^n + T_N^n + T_S^n\right)$$
$$+ \left(\frac{1}{\Delta t} - \frac{2\eta_1}{h^2} - \frac{\eta_1}{2}\right)T_P^n + \eta_2 T_a + \eta_3. \quad (3)$$

By rearranging the terms of Eq. (3) and writing it in the classical form of the discretized equation in terms of the matrix coefficients, we have

$$A_P T_P^{n+1} = A_E\left(T_E^{n+1} + T_E^n\right) + A_w\left(T_W^{n+1} + T_W^n\right) + A_N\left(T_N^{n+1} + T_N^n\right) + A_S\left(T_S^{n+1} + T_S^n\right) + A_{Pa}T_P^n + \eta_2 T_a$$
$$+ \eta_3$$
$$(4)$$

in which the coefficients are given by,

$$A_E = A_W = A_N = A_S = \frac{\eta_1}{2h^2}, \quad A_P = \frac{1}{\Delta t} + \frac{\eta_2}{2} + \frac{2\eta_1}{h^2}, \quad (5)$$

$$A_{Pa} = \frac{1}{\Delta t} - \frac{\eta_2}{2} - \frac{2\eta_1}{h^2} \quad and \quad b_P = A_{Pa}T_P^n + \eta_2 T_a + \eta_3 . \quad (6)$$

At the boundary points, the coefficients are given by $a_E = a_W = a_N = a_S = 0$, $a_P = 1$, and $b_p = T_{PC}$, where T_{PC} is the value of T at each point of the contour (see Figure 1).

The coefficients given by Eqs. (5) and (6), with their corresponding coefficients in the contour, form a system of linear equations of dimensions N_x and N_y of the form $AT = b$ with five diagonals, which is solved using the solver proposed in this work, described in the next section. The skin temperature on the boundary is approximated using Neumann, as follows: $T_{PC} = T_E + h\frac{q_0}{k}$, $T_{PC} = T_W$, $T_{PC} = T_S$, and $T_{PC} = T_N$ on the left, right, superior, and inferior boundaries,
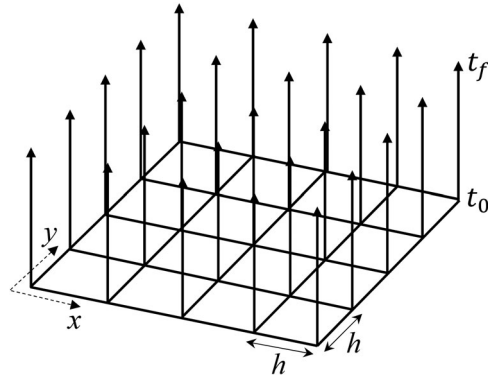
Figure 2. Waveform relaxation method scheme.

respectively. In this case, q_0 is the heat flow applied to the skin. The index PC indicates the point over the contour and E, W, S, and P indicate the surrounding points inside the domain.

2.3. WRMG solver

In this section, we describe a solver based on the so-called multigrid Waveform Relaxation Method (WRMG), proposed to solve the linear systems $AT = b$, given by Eqs. (4)–(6), generated from the discretization of the Pennes' bioheat equation.

For nonsteady state problems, the WR algorithms differ from standard time sweep methods (Time-Stepping) because their iterates are functions in time [24, 25]. The Partial Differential Equations (PDEs) are transformed into a large set of Ordinary Differential Equations (ODEs), and an iterative algorithm can be used to solve this system, where at each of the spatial points an ODE is solved at all time steps (see Figure 2).

The numerical solution has a high computational cost as it needs to solve systems of large dimensions. Each temporal ODEs must be solved in all spatial nodes separately, where the update of unknowns can be performed at the end of a WR cycle. Thus, we have an iterative method of repeating the procedure until a stopping criterion is reached. We can obtain a fully parallelizable method in space by using a colored ordering scheme [25, 43].

Based on Franco et al. [23], the proposed iterative algorithm considers a red-black Gauss-Seidel smoother in space and a line Gauss-Seidel smoother in time to solve the mathematical model described by Eq. (1) associated with the Crank-Nicolson methods.

Additionally, a coarse-grid correction procedure in the spatial dimension can accelerate the convergence of the red-black Gauss-Seidel Waveform Relaxation. The procedure consists in applying the standard multigrid algorithm [17, 18] to the system of ODEs obtained after the semi-discretization of the PDE problem.

The proposed algorithm is based on a two-grid cycle, which performs the following steps:

- Apply ν_1 iterations of a classical iterative method, called smoother, on the target fine grid Ω^h (pre-smoothing step).
- Compute the current fine grid approximation residual and restrict it to the coarse grid Ω^{2h} by using a restriction operator R_h^{2h}.
- Solve the residual equation on the coarse grid.
- Interpolate the obtained correction to the fine grid h using a prolongation operator P_{2h}^h and add the interpolated correction to the current fine grid approximation.
- Apply ν_2 iterations of a classical iterative method (post-smoothing step).

Table 1. Physical parameters of the skin for the verification code.

Properties of skin	Parameters	Value
Temperature of arterial blood (°C)	T_a	37
Density of skin tissue (kg m^{-3})	ρ_t	1,190
Specific heat of blood (J kg^{-1}K^{-1})	c_b	3,600
Blood perfusion rate (m^{3}s^{-1}m^{-3})	ω_b	0.1
Specific heat of skin tissue (J kg^{-1}K^{-1})	c_t	3,600
Density of blood (kg m^{-3})	ρ_b	1,060
Thermal conductivity of skin tissue (W m^{-1} K)	κ	0.235
Metabolic heat generation in the skin tissue (W m^{-3})	q_{met}	368.1
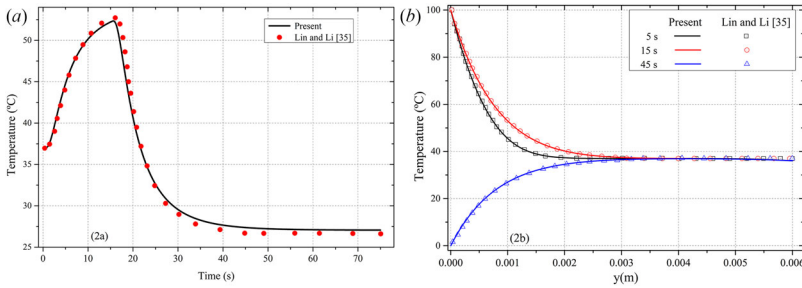
Figure 3. Comparison of temperature profiles: (a) over time and considering depth of 0.001 mm of skin; (b) along the y-axis considering final times of 5, 15 and 45 seconds.

The standard multigrid algorithm is obtained by recursively applying the same algorithm using a hierarchy of coarser grids, given by 2^L+1, where L is the space and time grid level, L = 1, 2, 3, …. Note that for $L = 10$, we have 1,025 nodes in the grid. This choice is due to the coarsening ratio of the multigrid method. An algorithm for WRMG is presented in [23].

This work considers standard full-weighting restriction and linear interpolation as the intergrid transfer operators [17]. There are different types of cycles based on how the grid is swept, for instance, the V-, W-, or F-cycles. We use the $V(\nu_1, \nu_2)$-cycle, where ν_1 and ν_2 are the numbers of pre- and post-smoothing, that is, the number of iterations in the restriction and prolongation process, respectively.

3. Results and discussion

3.1. Numerical code verification

Several studies on heat transfer perform a thermal analysis of human skin. However, as highlighted in [5], most use a one-dimensional approach. This work considers the same physical parameters for skin tissue from the analytical solution given by Lin and Li [40] to verify the proposed methodology for the numerical solution (Table 1). The authors developed a nonsteady state, one-dimensional analytical solution of bioheat transfer in skin tissue with general boundary conditions. The computational code was written in FORTRAN 95 with double-precision compiler, using the Intel FORTRAN Composer XE 2013. All calculations presented herein were performed on a desktop computer equipped with an Intel Core i7-9700 CPU 3.00GHz processor, Windows 10 Pro operating system, and 24-GB RAM 2.4-GHz DIMM.

Simulations were performed using a grid of $N = N_x N_y = 513 \times 513$ points in space, and $N_t = 2,048$ time steps to verify the consistency of the multigrid method with the Waveform Relaxation code. The initial skin temperature is assumed to be $T(x,0) = 37°C$ in a domain with $\ell = 6$ mm. Figure 3a compares the temperature profile over time, considering a depth of 1 mm of the skin tissue surface. In this case, on the tissue's surface (contour), we assume $T = 100°C$ when the

Table 2. Physical parameters of the skin for the case study.

Properties of skin	Parameters	Value
Density of skin tissue (kg m^{-3})	ρ_t	1,050
Specific heat of blood (J kg^{-1}K^{-1})	c_b	3,770
Blood perfusion rate (m^{3}s^{-1}m^{-3})	ω_b	0.01785
Metabolic heat generation in the melanoma (W m^{-3})	q_{ext}	36,810

time is between 0 to 15 s and $T = 0°C$ when outside this range. Figure 3b shows the temperature profile along the y-axis for the total times of 5, 15, and 45 seconds.

The curves observed in Figure 3 demonstrate that our numerical method (multigrid with Waveform Relaxation) provides solutions as efficient as those presented by the analytical solution in Lin and Li [40]. Therefore, for the remainder of this work, we will focus on the performance analysis of the multigrid method.

3.2. Multigrid performance in a case study

As previously mentioned, several works in the literature suggest that dynamic behavior favors a more adequated detection of unhealthy skin regions than a steady state analysis. Iljaž et al. [44] showed that it is possible to obtain tumor parameters using exact static or dynamic measurement data. However, a dynamic approach proved better for inaccurate temperature data than the steady-state, which cannot capture minor temperature differences between healthy skin and the tumor. In Gomboc et al. [45], an experimental setup for an active cooling device for dynamic thermography is proposed to achieve a constant cooling temperature that induces deep cooling penetration and, therefore, better thermal contrast. Magalhaes et al. [7] collected and analyzed static and dynamic (cooling) thermal images of melanoma and melanocytic nevi lesions to retrieve thermal parameters particular to these skin lesions. The steady-state and dynamic variables were tested separately using different machine learning classifiers to verify whether the distinction between melanoma and nevi lesions was achievable. The differentiation of both skin tumors was doable, with an accuracy of 84.2% and a sensitivity of 91.3% after implementing a learner based on support vector machines and an input vector composed of static variables.

In this context, we simulated a transient case study inspired by the work of Cheng and Herman [46], in which the region of interest is cooled, generally up to 15 °C, and then the behavior of the elevation in skin temperature is observed. In this dynamic process, the temperature differences between healthy and unhealthy regions increases, facilitating the diagnosis. We used a 30mm-diameter melanoma for the simulations. Its physical properties are presented in Table 2, and the other parameters are the same as in Table 1. Figure 4 shows the results of these simulations in which are given the temperature distribution for the time instants of 30 s, 60 s, 120 s, and in steady-state with a grid of $N = N_x\ N_y = 1,025 \times 1,025$ points in space and $N_t = 1,024$ time steps is also displayed.

Hundreds of simulations for the dynamic case were done to evaluate the performance of the multigrid method in the studied problem, Eq. (1). The influence on the CPU time was also measured for the number of inner iterations of the $V(\nu_1, \nu_2)$-cycle.

Figure 5 shows the change in CPU time according to the number of inner iterations in the restriction and prolongation, ν_1 and ν_2, for the red-black Gauss-Seidel smoother, using two grid sizes, $N = 257 \times 257$ and $N = 129 \times 129$ points, with ten levels in the time direction of the Waveform Relaxation Method. The tests were performed for three heating times in the melanoma region, 5 s, 30 s, and 120 s. The results demonstrate excellent method stability from the point of view of the number of inner iterations. For all simulations (Figures 5a–5f), both in the restriction and prolongation, the optimal values of ν_1 and ν_2 were the same. This behavior was also
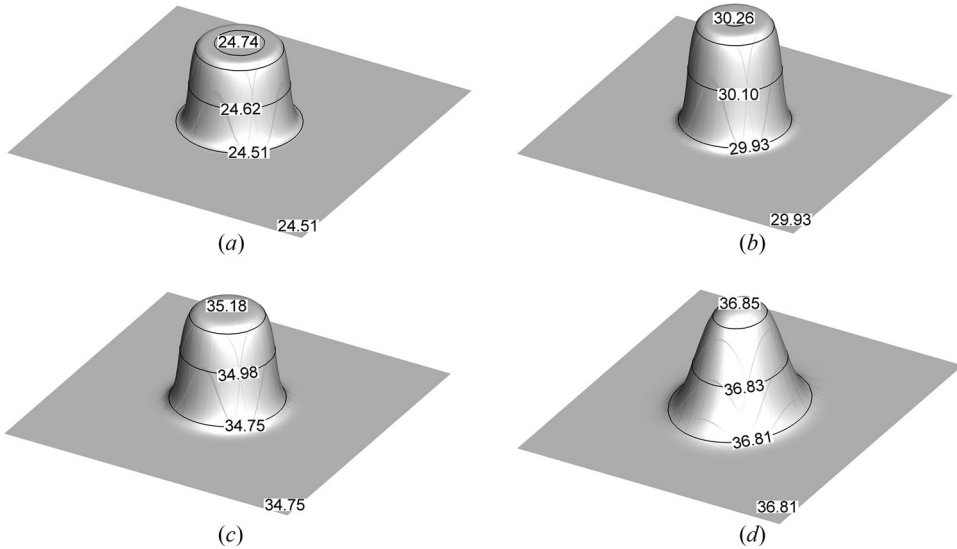
Figure 4. Thermal recovery for (a) 30 s, (b) 60 s, (c) 120 s, (d) steady state. Temperature given in degrees Celsius.

observed in other grids. Thus, we can infer that the heating time and grid size do not influence the number of inner iterations.

Figure 6 illustrates the number of V-cycles as a function of the number of levels in time required to reach convergence and the average convergence rate as a function of the number of grid levels. Importantly, $N_t = 2^L + 1$, where L is the number of levels in time, within the scope of the multigrid method. Figure 6a shows the variable L ranging from 2 to the maximum value possible in the computational memory limit. In this analysis, three fine spatial grids were used, $N = 129 \times 129$, $N = 257 \times 257$, and $N = 513 \times 513$. Note that the number of V-cycles increases in the first few levels in time, but there is also a decrease to 8 cycles for the grid $N = 129 \times 129$, and 9 cycles for the grid $N = 257 \times 257$. Figure 6b shows the grid levels from 2 to 10 and the increase in V-cycles until stability, at 12. In this analysis, we set $N = N_x N_y$, that is, $N = 5 \times 5$, ..., $1,025 \times 1,025$ points, corresponding to 10 grid levels, and the number of levels in time at 10, that is, $N_t = 1,025$ time step. Results confirm that the number of cycles grows with the increase in grid size to up to a maximum of 12 cycles in the finest grid, where stability is expected, which is a characteristic of the multigrid method for most problems, as shown in [17].

3.3. Average convergence factor—ρ_m

The convergence factor is an indicator for most iterative methods. It can be used to indicate the efficiency of an algorithm or to compare the computational performance of two or more methods. In the present work, the average convergence factor is given by $\rho_m = \sqrt[it]{\|R^{it}\|_\infty / \|R^0\|_\infty}$, where $\|R^{it}\|_\infty$ is the infinite norm of the residual in the it-th iteration, see [47]. Conversely, the parameter $\lambda = \Delta t / \Delta x^2$ can be considered a measure of the degree of anisotropy and strongly influences the matrix coefficients, affecting the method's performance. The ρ_m parameter can be used to find the λ intervals in which multigrid and singlegrid methods are more efficient. This analysis is done for different grids, as seen in Figure 7.

The simulations were carried out for spatial grids $N = 65 \times 65$ and $N = 129 \times 129$, with N_t ranging from 17 to 8,193; and for $N = 257 \times 257$, with N_t ranging from 17 to 2,049.

Figure 7a shows that the variable ρ_m is a worse factor in the singlegrid than in the multigrid in all the three grid sizes analyzed. In the multigrid method, ρ_m presents small values for all $\log_2(\lambda)$, obtaining better convergence factors. Note that for the grids used, the convergence
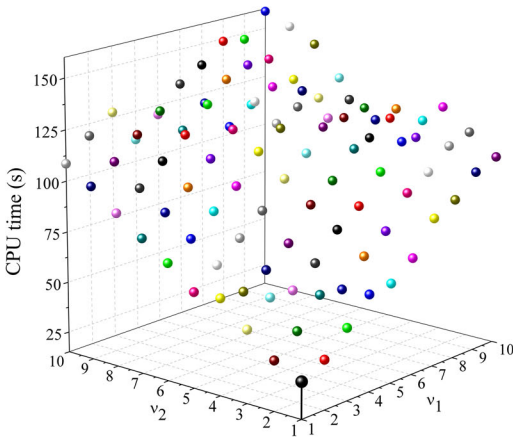
(a) Heating time 5 s.
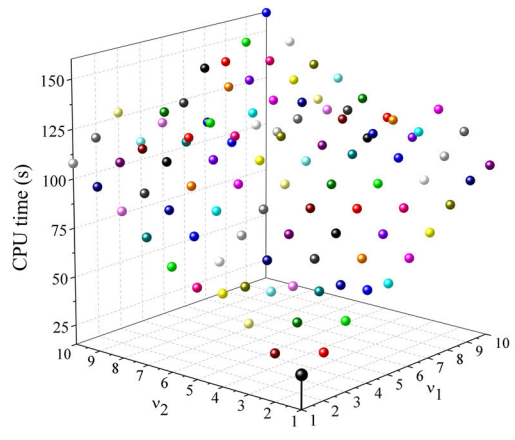
(b) Heating time 30 s.
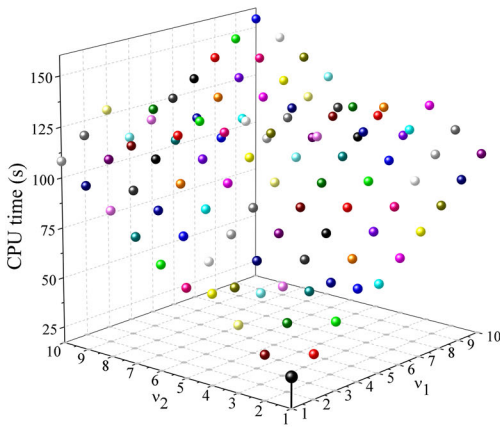
(c) Heating time 120 s.
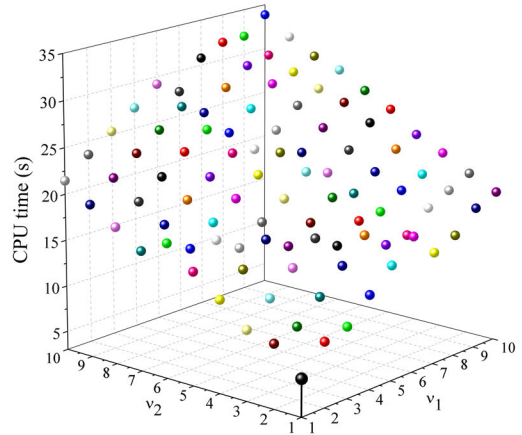
(d) Heating time 5 s.
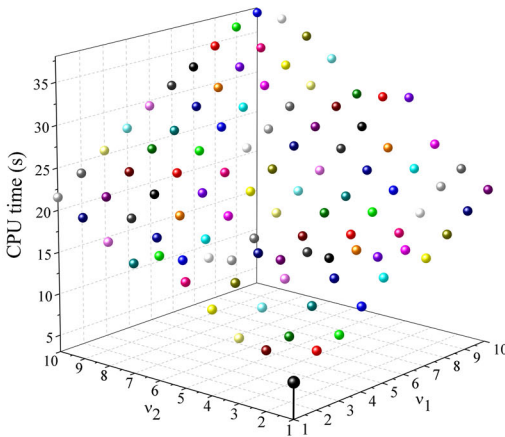
(e) Heating time 30 s.
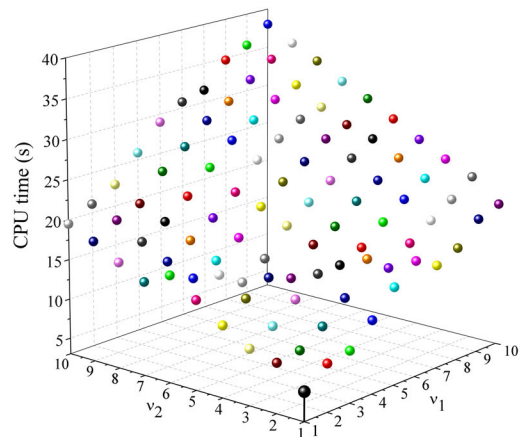
(f) Heating time 120 s.

Figure 5. CPU time vs. number of inner iterations of solver to different grids and heating times. The Figures (a)-(c) refer to 257×257 grid and the Figures (d)–(f) refer to 129×129 grid.

factor of the multigrid method remains stable, indicating the grid independence of this method combined with the Waveform Relaxation. Figure 7b demonstrates the increase in the average convergence factor according to the grid size, showing possible stability close to 0.13.
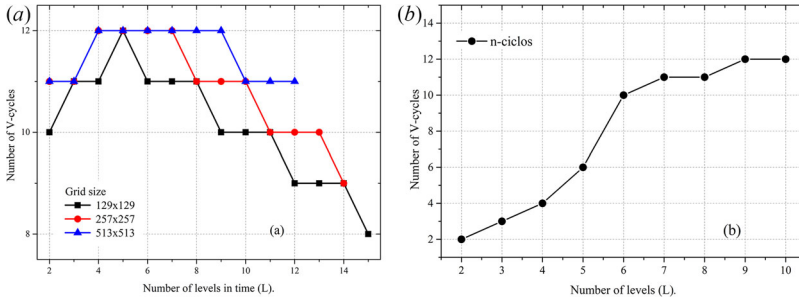
Figure 6. Number of *V*-cycles (a) as a function the number of levels in time for three grids, (b) as function of the number of levels in space with the number of levels in the fixed time at most.
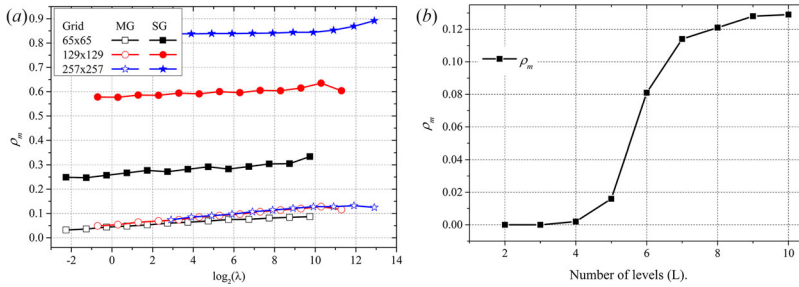
Figure 7. Average convergence factor ρ_m vs.: (a) $\log_2(\lambda)$, (b) number of levels in time.
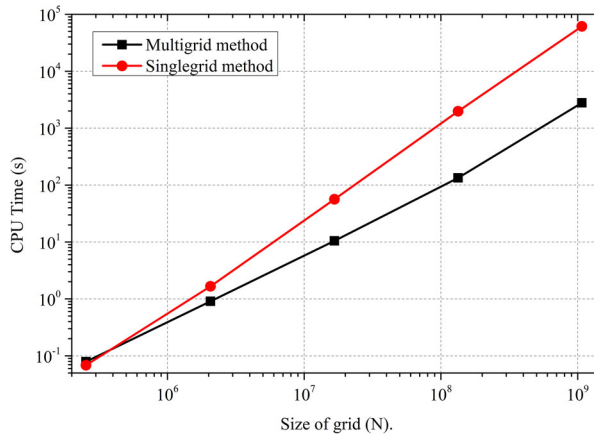
Figure 8. Multigrid and singlegrid performance with grids up to $1,025 \times 1,025$ and $N_t = N$.

When analyzing the influence of the size of the problem on the CPU time, the optimal numbers of inner iterations in the restriction and prolongation (ν_1, ν_2) should be considered. In this analysis, we assume grid sizes of $N = N_x N_y = 3 \times 3$ up to the highest grid size supported by the computer's physical memory used, $N = 1,025 \times 1,025$, and $N_t = N_x$ for all grid levels. Figure 8 shows the results obtained using the singlegrid method (SG) associated with the red-black Gauss-Seidel smoother on a logarithmic scale. Coarser grids ($N < 33 \times 33$ points) presented CPU times close to zero for the multigrid and singlegrid methods. In this analysis, the efficiency of the multigrid method is evident. Its advantage over the singlegrid method grows with the increase in the number of points in the grid, as stated in other works using different mathematical models [48, 49]. One can also observe that at $N = 1,025 \times 1,025$, the multigrid is approximately 30 times faster than the singlegrid method. The results are also better than those in [5], in

Table 3. Coefficient c and expoent p for Eq. (7), with $N = 1,025 \times 1,025$, several N_t and Pennes Equation with red-black Gauss-Seidel solver.

N_t	Multigrid		Singlegrid	
	c	p	c	p
129	$4.86E - 07$	1.0019	$2.38E - 06$	1.73461
257	$2.38E - 06$	0.95594	$1.88E - 11$	1.78303
513	$1.46E - 06$	1.05651	$8.26E - 12$	1.91402

which the same problem was solved using the standard Time-Stepping methodology. Figure 8 shows that the solution method proposed using multigrid waveform can be an exciting alternative for dynamics simulation in inverse problems and data generation for machine learning.

3.4. Computational effort

To determine the order of complexity of the solver and the behavior of the curve with the CPU time, we use a geometric curve fit by the least square method given by

$$t_{CPU}(N_T) = cN_T^p \tag{7}$$

where $N_T = NN_t$ is the total number of points, p represents the order of complexity of the solver associated with the method employed (or the inclination of each curve in Figure 8), and c is a coefficient that depends on the adopted method and solver. Theoretically, p values close to one represent better performances of the employed algorithm [17]. Ideally, the value of p for the multigrid method is $p = 1$; which means the CPU time increases linearly with the size of the grid.

Table 3 presents the coefficients c and exponents p for Eq. (7) obtained for Pennes' equation (discretized with $N = N_x N_y = 1,025 \times 1,025$ and several N_t) and red-black Gauss-Seidel smoother. The results confirm that the CPU time of the multigrid method with the red-black Gauss-Seidel smoother grows almost linearly with the increasing N_T. Values of $p \approx 1$ for multigrid and $p \approx 2$ for singlegrid method agree with the theoretical values [17].

In addition to comparing the MGWR with the conventional singlegrid method (Figure 8 and Table 3), the multigrid method is a tool to solve large linear systems generated from any numerical solutions such as Finite Element, Finite Volume, and others numerical methods [17].

MGWR is robust as it uses the standard coarsening in the space and the line-in-time solver [50]. It is also efficient because it has good convergence factors and is parallelizable.

4. Conclusions

An efficient multigrid Waveform Relaxation Method based on a red-black Gauss-Seidel smoother in space and line Gauss-Seidel smoother in time was proposed to solve the Pennes' bioheat equation. The derivatives were approximated using the Finite Difference Method in a uniform grid, with a five-point second-order central difference scheme accurate in space and the Crank-Nicolson scheme in the temporal derivative. Two-dimensional numerical experiments are presented, showing the satisfactory performance of the proposed algorithm for the well-known thermal analysis of human skin. The analysis of the multigrid method was carried out with different space and time grid sizes. Considering the average convergence factor and computational cost, the multigrid Waveform Relaxation Method shows optimal efficiency in addition to the great advantage of a parallel computing approach, proposed in this work.

Acknowledgments

Disclosure statement

We declare that we do not have any commercial or associative interest that represents a conflict of interest in connection with the work submitted.

ORCID

Cosmo D. Santiago http://orcid.org/0000-0001-6971-0586
Gylles R. Ströher http://orcid.org/0000-0002-1164-9038
Marcio A. V. Pinto http://orcid.org/0000-0003-4166-4674
Sebastião R. Franco http://orcid.org/0000-0002-4580-5924

References

[1] M. Anbar, "Clinical thermal imaging today," *IEEE Eng. Med. Biol. Mag.*, vol. 17, no. 4, pp. 25–33, 1998. DOI: 10.1109/51.687960.

[2] R. Lawson, "Implications of surface temperatures in the diagnosis of breast cancer," *Can. Med. Assoc. J.*, vol. 75, no. 4, pp. 309–311, 1956.

[3] F. Xu and T. J. Lu, *Introduction to Skin Biothermomechanics and Thermal Pain*. 1st ed. Beijing, China: Springer, 2011, 209–220. DOI: 10.1007/978-3-642-13202-5.

[4] L. F. A. S. Zafanelli, G. L. Ströher, and G. R. Ströher, "Numerical thermal analysis of human skin subjected to conditions of exams thermal mapping dynamic and not dynamic," *Engevista*, vol. 19, no. 4, p. 1121, 2017. DOI: 10.22409/engevista.v19i4.933.

[5] G. R. Ströher and C. D. Santiago, "Numerical two-dimensional thermal analysis of the human skin using the multigrid method," *Acta Sci. Technol.*, vol. 42, no. 1, p. e40992, 2020. DOI: 10.4025/actascitechnol.v42i1.40992.

[6] G. R. Ströher and G. L. Ströher, "Numerical thermal analysis of skin tissue using parabolic and hyperbolic approaches," *Int. Commun. Heat Mass Transf.*, vol. 57, pp. 193–199, 2014. DOI: 10.1016/j.icheatmasstransfer.2014.07.026.

[7] C. Magalhaes, R. Vardasca, and J. Mendes, "Recent use of medical infrared thermography in skin neoplasms," *Skin Res. Technol.*, vol. 24, no. 4, pp. 587–591, 2018. DOI: 10.1111/srt.12469.

[8] C. Herman, "The role of dynamic infrared imaging in melanoma diagnosis," *Expert Rev. Dermatol.*, vol. 8, no. 2, pp. 177–184, 2013. DOI: 10.1586/edm.13.15.

[9] S. E. Godoy, M. M. Hayat, D. A. Ramirez, S. A. Myers, R. S. Padilla, and S. Krishna, "Detection theory for accurate and non-invasive skin cancer diagnosis using dynamic thermal imaging," *Biomed. Opt. Express*, vol. 8, no. 4, pp. 2301–2323, 2017. DOI: 10.1364/BOE.8.002301.

[10] H. Chen, K. Wang, Z. Du, W. Liu, and Z. Liu, "Predicting the thermophysical properties of skin tumor based on the surface temperature and deep learning," *Int. J. Heat Mass Transf.*, vol. 180, p. 121804, 2021. DOI: 10.1016/j.ijheatmasstransfer.2021.121804.

[11] J. P. Agnelli, A. A. Barrea, and C. V. Turner, "Tumor location and parameter estimation by thermography," *Math. Comput. Modell.*, vol. 53, no. 7–8, pp. 1527–1534, 2011. DOI: 10.1016/j.mcm.2010.04.003.

[12] J. H. Holland, "Outline for a logical theory of adaptive systems," *J. ACM*, vol. 9, no. 3, pp. 297–314, 1962. DOI: 10.1145/321127.321128.

[13] L. M. Gambardella and M. Dorigo, "Solving symmetric and asymmetric TSPs by ant colonies," Proceedings of IEEE International Conference on Evolutionary Computation, 1996. pp. 622–627. DOI: 10.1109/ICEC.1996.542672.

[14] G. R. Ströher and G. L. Ströher, "Algoritmo de otimização metaheurística inspirado em um jogo de basquete," in *Engenharia de Produção e a Indústria 4.0*, 1st ed. Ponta Grossa, Brazil: AYA EDITORA, 2020, pp. 61–73. DOI: 10.47573/aya.88580.2.3.4.

[15] J. E. Dennis and V. J. Torczon, "Derivative-free pattern search methods for multidisciplinary design problems," 5th Symposium on Multidisciplinary Analysis and Optimization, Panama, City Beach, FL, USA,

1994. American Institute of Aeronautics and Astronautics. Published Online in 2012. DOI: 10.2514/6.1994-4349.

[16] M. R. Rossi, D. Tanaka, K. Shimada, and Y. Rabin, "An efficient numerical technique for bioheat simulations and its application to computerized cryosurgery planning," *Comput. Methods Programs Biomed.*, vol. 85, no. 1, pp. 41–50, 2007. DOI: 10.1016/j.cmpb.2006.09.014.

[17] U. Trottenberg, C. W. Oosterlee, and A. Schuller, *Multigrid*. London, UK: Academic Press, 2001.

[18] P. Wesseling, *An Introduction to Multigrid Methods*. Chichester: Wiley, 1992.

[19] N. Sarkar, "On a new time-fractional order Bio-Heat transfer model," Int. Res. J. Eng. Technol. (IRJET), 2015. Available: https://www.irjet.net/archives/V2/i4/Irjet-v2i4193.pdf. Accessed: Jul. 19, 2022.

[20] A. Belmiloudi, "Parameter identification problems and analysis of the impact of porous media in biofluid heat transfer in biological tissues during thermal therapy," *Nonlinear Anal.: Real World Appl.*, vol. 11, no. 3, pp. 1345–1363, 2010. DOI: 10.1016/j.nonrwa.2009.02.025.

[21] S. Ghosh, T. Das, S. Chakraborty, and S. K. Das, "Predicting DNA-mediated drug delivery in interior carcinoma using electromagnetically excited nanoparticles," *Comput. Biol. Med.*, vol. 41, no. 9, pp. 771–779, 2011. DOI: 10.1016/j.compbiomed.2011.06.013.

[22] N. Sahoo, S. Ghosh, A. Narasimhan, and S. K. Das, "Investigation of non-Fourier effects in bio-tissues during laser-assisted photothermal therapy," *Int. J. Therm. Sci.*, vol. 76, pp. 208–220, 2014. DOI: 10.1016/j.ijthermalsci.2013.08.014.

[23] S. R. Franco, C. Rodrigo, F. J. Gaspar, and M. A. V. Pinto, "A multigrid waveform relaxation method for solving the poroelasticity equations," *Comp. Appl. Math.*, vol. 37, no. 4, pp. 4805–4820, 2018. DOI: 10.1007/s40314-018-0603-9.

[24] M. J. Gander, "50 Years of Time Parallel Time Integration," in *Multiple Shooting and Time Domain Decomposition Methods. Contributions in Mathematical and Computational Sciences*, vol. 9, T. Carraro, M. Geiger, S. Körkel, and R. Rannacher, Eds. Heidelberg, Germany: Springer, 2015. DOI: 10.1007/978-3-319-23321-5_3.

[25] S. Vandewalle, *Parallel Multigrid Waveform Relaxation for Parabolic Problems*. Stuttgar: Springer-Verlag, 2013.

[26] J. Liu and Y.-L. Jiang, "Waveform relaxation for reaction–diffusion equations," *J. Comput. Appl. Math.*, vol. 17, pp. 5040–5055, 2011. DOI: 10.1016/j.cam.2011.04.035.

[27] H. Ltaief and M. Garbey, "A parallel Aitken-additive Schwarz waveform relaxation suitable for the grid," *Parallel Comput.*, vol. 35, no. 7, pp. 416–428, 2009. DOI: 10.1016/j.parco.2009.05.001.

[28] X. Antoine and E. Lorin, "A Schwarz waveform relaxation method for time-dependent space fractional Schrödinger/heat equations," *Appl. Numer. Math.*, vol. 182, pp. 248–264, 2022. DOI: 10.1016/j.apnum.2022.07.012.

[29] X. Hu, C. Rodrigo, and F. J. Gaspar, "Using hierarchical matrices in the solution of the time-fractional heat equation by multigrid waveform relaxation," *J. Comput. Phys.*, vol. 416, p. 109540, 2020. DOI: 10.1016/j.jcp.2020.109540.

[30] H. H. Pennes, "Analysis of tissue and arterial blood temperatures in the resting human forearm," *J. Appl. Physiol.*, vol. 1, no. 2, pp. 93–122, 1948. DOI: 10.1152/jappl.1948.1.2.93.

[31] V. S. Kublanov, V. I. Borisov, and M. V. Babich, "Simulation the distribution of thermodynamic temperatures and microwave radiation of the human head," *Comput. Methods Programs Biomed.*, vol. 190, p. 105377, 2020. DOI: 10.1016/j.cmpb.2020.105377.

[32] G. Bellizzi, O. M. Bucci, and G. Chirico, "Numerical assessment of a criterion for the optimal choice of the operative conditions in magnetic nanoparticle hyperthermia on a realistic model of the human head," *Int. J. Hyperth.*, vol. 32, no. 6, pp. 688–703, 2016. DOI: 10.3109/02656736.2016.1167258.

[33] S. Kamangar, M. A. Khan, I. A. Badruddin, T. M. Yunus Khan, and N. Ghazali, "Numerical analysis of heat transfer in the human head," *J. Mech. Sci. Technol.*, vol. 33, no. 7, pp. 3597–3605, 2019. DOI: 10.1007/s12206-019-0654-x.

[34] K. Das and S. C. Mishra, "Non-invasive estimation of size and location of a tumor in a human breast using a curve fitting technique," *Int. Commun. Heat Mass Transf.*, vol. 56, pp. 63–70, 2014. DOI: 10.1016/j.icheatmasstransfer.2014.04.015.

[35] J. L. Gonzalez-Hernandez, A. N. Recinella, S. G. Kandlikar, D. Dabydeen, L. Medeiros, and P. Phatak, "Technology, application and potential of dynamic breast thermography for the detection of breast cancer," *Int. J. Heat Mass Transf.*, vol. 131, pp. 558–573, 2019. DOI: 10.1016/j.ijheatmasstransfer.2018.11.089.

[36] A. Lozano, J. C. Hayes, L. M. Compton, J. Azarnoosh, and F. Hassanipour, "Determining the thermal characteristics of breast cancer based on high-resolution infrared imaging, 3D breast scans, and magnetic resonance imaging," *Sci. Rep.*, vol. 10, no. 1, p. 10105, 2020. DOI: 10.1038/s41598-020-66926-6.

[37] S. Singh and R. Repaka, "Parametric sensitivity analysis of critical factors affecting the thermal damage during RFA of breast tumor," *Int. J. Therm. Sci.*, vol. 124, pp. 366–374, 2018a. DOI: 10.1016/j.ijthermalsci.2017.10.032.

[38] S. Singh and R. Repaka, "Thermal characterization using fourier and non-fourier conduction during radio-frequency ablation of breast tumor," *MultScienTechn*, vol. 30, no. 2–3, pp. 207–219, 2018b. DOI: 10.1615/MultScienTechn.2018021352.

[39] H. Ahmadikia, R. Fazlali, and A. Moradi, "Analytical solution of the parabolic and hyperbolic heat transfer equations with constant and transient heat flux conditions on skin tissue," *Int. Commun. Heat Mass Transf.*, vol. 39, no. 1, pp. 121–130, 2012. DOI: 10.1016/j.icheatmasstransfer.2011.09.016.

[40] S. M. Lin and C. Y. Li, "Analytical solutions of non-Fourier bio-heat conductions for skin subjected to pulsed laser heating," *Int. J. Therm. Sci.*, vol. 110, pp. 146–158, 2016. DOI: 10.1016/j.ijthermalsci.2016.06.034.

[41] J. M. Luna, A. H. Guerrero, R. R. Méndez, and J. L. L. Ortiz, "Solution of the inverse bio-heat transfer problem for a simplified dermatological application: case of skin cancer," *Ingenier. Mecáni. Tecnolog. Desarroll.*, vol. 4, pp. 219–228, 2014.

[42] T. C. Shih, P. Yuan, W. L. Lin, and H. S. Kou, "Analytical analysis of the Pennes bioheat transfer equation with sinusoidal heat flux condition on skin surface," *Med. Eng. Phys.*, vol. 29, no. 9, pp. 946–953, 2007. DOI: 10.1016/j.medengphy.2006.10.008.

[43] D. Conte, R. D'Ambrosio, and B. Paternoster, "GPU-acceleration of waveform relaxation methods for large differential systems," *Numer. Algor.*, vol. 71, no. 2, pp. 293–310, 2016. DOI: 10.1007/s11075-015-9993-6.

[44] J. Iljaž, L. C. Wrobel, M. Hriberšek, and J. Marn, "The use of Design of Experiments for steady state and transient inverse melanoma detection problems," *Int. J. Therm. Sci.*, vol. 135, pp. 256–275, 2019. DOI: 10.1016/j.ijthermalsci.2018.09.003.

[45] T. Gomboc, J. Iljaž, L. C. Wrobel, M. Hriberšek, and J. Marn, "Design of constant temperature cooling device for melanoma screening by dynamic thermography," *Eng. Anal. Boundary Elem.*, vol. 125, pp. 66–79, 2021. DOI: 10.1016/j.enganabound.2021.01.009.

[46] T. Y. Cheng and C. Herman, "Analysis of skin cooling for quantitative dynamic infrared imaging of near-surface lesions," *Int. J. Therm. Sci.*, vol. 86, pp. 175–188, 2014. DOI: 10.1016/j.ijthermalsci.2014.06.033.

[47] W. L. Briggs, V. E. Henson, and S. F. Mccormick, *A Multigrid Tutorial*, 2th ed. Philadelphia, USA: SIAM, 2000.

[48] C. D. Santiago, C. H. Marchi, and L. F. Souza, "Performance of geometric multigrid method for coupled two-dimensional systems in CFD," *Appl. Math. Modell.*, vol. 39, no. 9, pp. 2602–2616, 2015. DOI: 10.1016/j.apm.2014.10.067.

[49] F. Oliveira, S. R. Franco, and M. A. V. Pinto, "The effect of multigrid parameters in a 3D heat diffusion equation," *Int. J. Appl. Mech. Eng.*, vol. 23, no. 1, pp. 213–221, 2018. DOI: 10.1515/ijame-2018-0012.

[50] C. A. Thole and U. Trottenberg, "Basic smoothing procedures for the multigrid treatment of elliptic 3D operators," *Appl. Math. Comput.*, vol. 19, no. 1–4, pp. 333–345, 1986. Pages. DOI: 10.1016/0096-3003(86)90112-8.